Materials Today Bio 31 (2025) 101629

Contents lists available at ScienceDirect

Materials Today Bio

journal homepage: www.journals.elsevier.com/materials-today-bio

Peptide-modified mesoporous silica nanoparticles for the coordinated regulation of macrophage polarization and pyroptosis in the treatment of implant-related infections

Zhi Li [a,1], Yuhang Wang [a,1], Xingshi Yuan [a,1], Mingyou Xu [a], Xiaofang Wang [b], Chang Liu [c], Chen Zhu [a,*], Wei Pei [d,**], Jiaxiang Bai [a,***], Xifu Shang [a,****]

[a] Department of Orthopedics, Centre for Leading Medicine and Advanced Technologies of IHM, The First Affiliated Hospital of USTC, Division of Life Sciences and Medicine, University of Science and Technology of China, Hefei, Anhui, 230001, China

[b] Department of Clinical Laboratory, The First Affiliated Hospital of USTC, Division of Life Sciences and Medicine, University of Science and Technology of China, Hefei, China

[c] Department of General Surgery, The Second Affiliated Hospital of Anhui Medical University, Hefei, Anhui, China

[d] Tongji University Cancer Center, Shanghai Tenth People's Hospital, School of Medicine, Tongji University, Shanghai, China

ARTICLE INFO

Keywords:
Pyroptosis
Macrophage polarization
Chronic infections
Implant-related infections (IRIs)

ABSTRACT

Implant-related infections (IRIs) present a significant challenge in clinical treatment because of the formation of biofilms. The complex architecture of biofilms not only impedes antibiotic penetration, fostering the evolution of multidrug resistance in bacteria under minimal selective pressure but also suppresses the antimicrobial activity of macrophages and induces their pyroptosis in large quantities. This excessive pyroptosis impairs the collective immune function of macrophages, enabling pathogens to evade immune system clearance and rendering infection difficult to eradicate. Existing treatment strategies often necessitate extensive surgical debridement, which not only causes significant harm to patients' physiological health and quality of life but also results in limited therapeutic outcomes. To address these challenges, this study developed a mesoporous silica nanoparticle system (MRL) modified with the RGD (Arginine-Glycine-Aspartic acid) tripeptide and loaded with the antimicrobial peptide LL-37. The LL-37 released from MRL can not only directly disrupt bacterial cell membranes, preventing bacteria from developing resistance through conventional mutation mechanisms, but also enhance antimicrobial activity by modulating macrophage polarization toward the M1 phenotype. However, LL-37 may induce and exacerbate macrophage pyroptosis within biofilms. Therefore, we modified the nanoparticles with RGD to increase macrophage viability and reduce their number of deaths, thereby alleviating the immunosuppression caused by excessive macrophage pyroptosis. In vitro and in vivo experiments demonstrated that MRL, while preserving the antimicrobial activity and immunomodulatory function of LL-37, significantly reduced macrophage pyroptosis and protected the collective immune activity of macrophages. Thus, the fine-tuned regulation of immune response was achieved, providing new insights and strategies for the treatment of IRIs.

1. Introduction

Biofilms are highly structured microbial communities that adhere to host tissues or abiotic surfaces. In implant-related infections (IRIs), bacteria colonize the surfaces of implanted medical devices and secrete an extracellular polymeric substance (EPS), forming a protective matrix [1–3]. This structured barrier enhances bacterial resistance to antibiotics and the host immune system, making the treatment of IRIs fundamentally distinct from that of common infections. For common infections, current treatment strategies rely primarily on the synergistic

* Corresponding authors.
** Corresponding author.
*** Corresponding authors.
**** Corresponding author.
E-mail addresses: zhuchena@ustc.edu.cn (C. Zhu), 2310940@tongji.edu.cn (W. Pei), jxbai1995@ustc.edu.cn (J. Bai), shangxifu@ustc.edu.cn (X. Shang).
[1] These authors contributed equally to this work.

https://doi.org/10.1016/j.mtbio.2025.101629
Received 9 January 2025; Received in revised form 14 February 2025; Accepted 2 March 2025
Available online 4 March 2025
2590-0064/© 2025 Published by Elsevier Ltd. This is an open access article under the CC BY-NC-ND license (http://creativecommons.org/licenses/by-nc-nd/4.0/).

action of antibiotics and the host immune system [4]. Antibiotics exert bactericidal or bacteriostatic effects by targeting specific bacterial life processes or structures, thereby disrupting bacterial survival and replication [5,6]. The host immune system recognizes pathogen-associated molecular patterns (PAMPs) on bacteria to activate macrophage Toll-like receptors (TLRs), promoting M1 polarization and the release of inflammatory cytokines such as interleukin-6 (IL-6), tumor necrosis factor-alpha (TNF-α), and interleukin-1β (IL-1β), thereby enhancing bactericidal activity [7–9]. Additionally, the host can trigger moderate pyroptosis while ensuring an adequate number of macrophages [10]. Pyroptosis induces macrophage membrane rupture and the release of abundant cytokines and inflammatory mediators, forming a robust immune barrier that effectively limits bacterial spread and growth [11]. However, in IRIs, biofilm formation greatly hinders infection control, fundamentally altering this situation. Patients often require multiple surgeries to completely eliminate infection foci [12–14].

Studies have shown that the difficulty in treating IRIs arises from the dual interference of biofilms with both antibiotics and the host immune response [15,16]. Regarding antibiotics, biofilms significantly reduce local drug concentrations by impeding antibiotic penetration, Thus providing a natural "shelter" for bacteria and serving as a breeding ground for multidrug-resistant strains [17]. In this environment, bacteria not only gradually develop resistance under low selective pressure but also accelerate the spread of resistance genes through horizontal gene transfer [18]. The development of drug-resistant bacteria severely undermines the therapeutic efficacy of existing antibiotics and significantly increases the risk of treatment failure and infection recurrence [19]. With regard to the host immune response, biofilms not only inhibit macrophage polarization toward the M1 phenotype but also induce excessive pyroptosis in macrophages on a large scale [20–22]. Unlike normal pyroptosis, excessive pyroptosis triggered by biofilms may temporarily increase local inflammation but result in substantial depletion of macrophages, drastically reducing their collective immune activity [23–25]. This dual interference ultimately enables pathogens within the biofilm to evade immune surveillance and establish persistent infections.

In response to these challenges, various innovative anti-infection strategies have been proposed in recent years. For instance, CeO_2@MSN, as a nanoplatform, integrates the antibacterial properties of cerium dioxide with the high surface area and stability of mesoporous silica, enabling efficient biofilm penetration and enhanced antimicrobial agent delivery [26]. However, its antibacterial efficacy primarily relies on electrostatic interactions between its positively charged surface and the biofilm, limiting its ability to actively modulate the host immune system. Additionally, another category of ultrasound-driven micro/-nanorobots (MNRs) utilizes ultrasound guidance to achieve precise navigation and targeted drug delivery to infected sites [27]. However, their complex material composition raises concerns regarding metabolism and long-term biocompatibility. More recently, studies have further proposed a microbubble-based ultrasound-stimulated exocytosis system (EMB-Hu), in which Fe_3O_4 nanoparticles are encapsulated within a red blood cell membrane [28]. This system enhances the penetration of antimicrobial agents into biofilms while simultaneously activating immune responses. However, the efficacy of EMB-Hu microbubbles is highly dependent on ultrasound energy regulation, and their penetration depth and localized precision may be limited in treating deep-seated infections. Furthermore, while the metal ions in these nanoparticles exhibit powerful antibacterial activity, their potential tissue toxicity remains a major limitation for clinical application. In contrast, antimicrobial peptides (AMPs), a class of novel antibiotic alternatives, have garnered significant attention due to their strong ability to penetrate biofilm matrices, low toxicity, and limited resistance development [29,30]. Among them, LL-37 is an endogenous human antimicrobial peptide with broad-spectrum antibacterial activity [31]. LL-37 directly disrupts bacterial cell membranes to exert antibacterial effects, making it difficult for bacteria to develop resistance through common mechanisms such as mutation or horizontal gene transfer [32]. Additionally, it can modulate macrophage polarization toward the M1 phenotype, thus alleviating the immune suppression induced by biofilms [33]. However, studies have shown that LL-37 may also induce pyroptosis in macrophages within the infection microenvironment, further exacerbating pyroptosis in macrophages within biofilms and leading to further depletion of macrophage populations [34]. Therefore, it is crucial to preserve antimicrobial and immunomodulatory functions of LL-37 while avoiding excessive pyroptosis.

To address these issues, we propose an innovative drug delivery strategy based on mesoporous silica nanoparticles (MSNs). Owing to their high surface area, large pore size, excellent biocompatibility, and functionalizable surface properties, MSNs have been widely used in the field of drug delivery applications [35,36]. In this study, LL-37 was loaded into MSNs, and its local concentration was controlled via physical sustained release, thereby reducing the risk of inducing macrophage pyroptosis. However, relying solely on physical sustained release is insufficient to precisely regulate the pyroptotic response of macrophages. To overcome this limitation, we further functionalized the MSNs surface by introducing RGD (arginine-glycine-aspartic acid) tripeptides. RGD is a cell-recognition sequence that binds to integrin receptors, facilitating the adhesion of MSNs to macrophages, increasing cell viability, and reducing cell death [37–39]. Therefore, we further functionalized the surface of MSNs with RGD tripeptides, with the goal of alleviating excessive pyroptosis in macrophages. Through this design, RGD-modified MSNs successfully reduced excessive pyroptosis in macrophages while preserving the antimicrobial and immunomodulatory functions of LL-37, thus protecting the host's immune defense and providing a novel approach for the treatment of IRIs.

2. Results and discussion

2.1. Synthesis and characterization of MRL

The synthesis of MRL is illustrated in Scheme 1. MSNs are widely used in drug delivery because of their excellent physicochemical properties, such as high specific surface area, tunable pore size, excellent chemical stability and biocompatibility. To synthesize MRL, MSNs were first aminated to obtain MSNs-NH_2. This modification endows the nanoparticles with greater chemical reactivity, forming the basis for subsequent synthesis reactions. Subsequently, RGD was grafted onto the surface of MSNs-NH_2 via an amidation reaction to produce MR, and LL-37 was successfully adsorbed into the mesopores and onto the surface of MR through electrostatic and hydrophobic interactions, resulting in the formation of the MRL complex. The morphology of the prepared nanoparticles was observed via transmission electron microscopy (TEM) (Fig. 1a). TEM images revealed that the MSNs exhibited excellent dispersibility, uniform size distribution, and a highly ordered mesoporous structure. As expected, after the addition of LL-37, the core color of the nanoparticles deepened, indicating that the particle density increased with the adsorption of LL-37. Moreover, MRL maintained a regular spherical structure and good dispersibility, suggesting that the modification and loading process had minimal impact on the structural stability of the material. Additionally, the diameters of 100 nanoparticles were measured via ImageJ software to analyze the size distribution. The average diameters of spherical MSNs and MSNs-NH_2 were approximately 75.93 nm and 75.53 nm, respectively, while the average diameter of MR increased to 77.24 nm. After the addition of LL-37, the average diameter of MRL increased to 106.26 nm (Fig. 1b). This result aligns with the increased density and further supports the successful assembly of LL-37 within the nanoparticles through surface adsorption and mesoporous loading. Next, the mesoporous structure of the material was characterized via N_2 adsorption-desorption isotherms. The isotherm for MR displayed a typical type IV characteristic (Fig. S1, Supporting Information), indicating a large pore volume, high specific surface area, and significant mesoporous structure. The corresponding mesopore

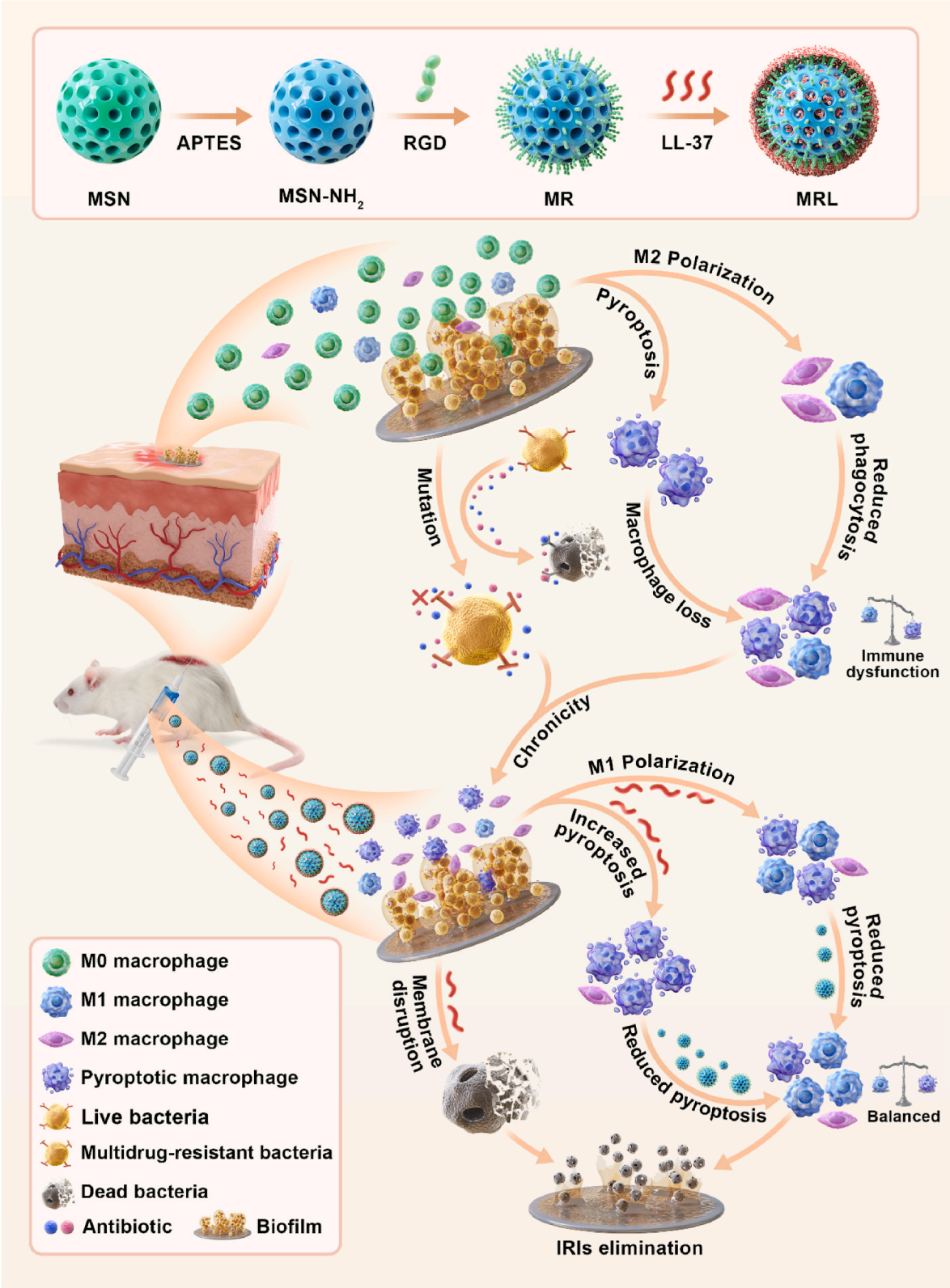

Scheme 1. Synthesis of mesoporous silica nanoparticles (MRL) modified with RGD and adsorbed with the antimicrobial peptide LL-37. MRL eradicated biofilms associated with implant-related infections through direct bactericidal and coordinated modulation of macrophage polarization and pyroptosis.

volume, Brunauer-Emmett-Teller (BET) specific surface area, and mesopore size were calculated to be 0.65 $cm^3\ g^{-1}$, 507.34 $m^2\ g^{-1}$, and 4.94 nm, respectively. The large mesoporous structure and high specific surface area provided more binding sites for LL-37, ensuring its uniform distribution on the material surface and within the mesopores. The mesoporous structure of MR also provides physical protection for LL-37, reducing its interaction with proteases in biological fluids and significantly enhancing its stability [40]. This protective mechanism enables

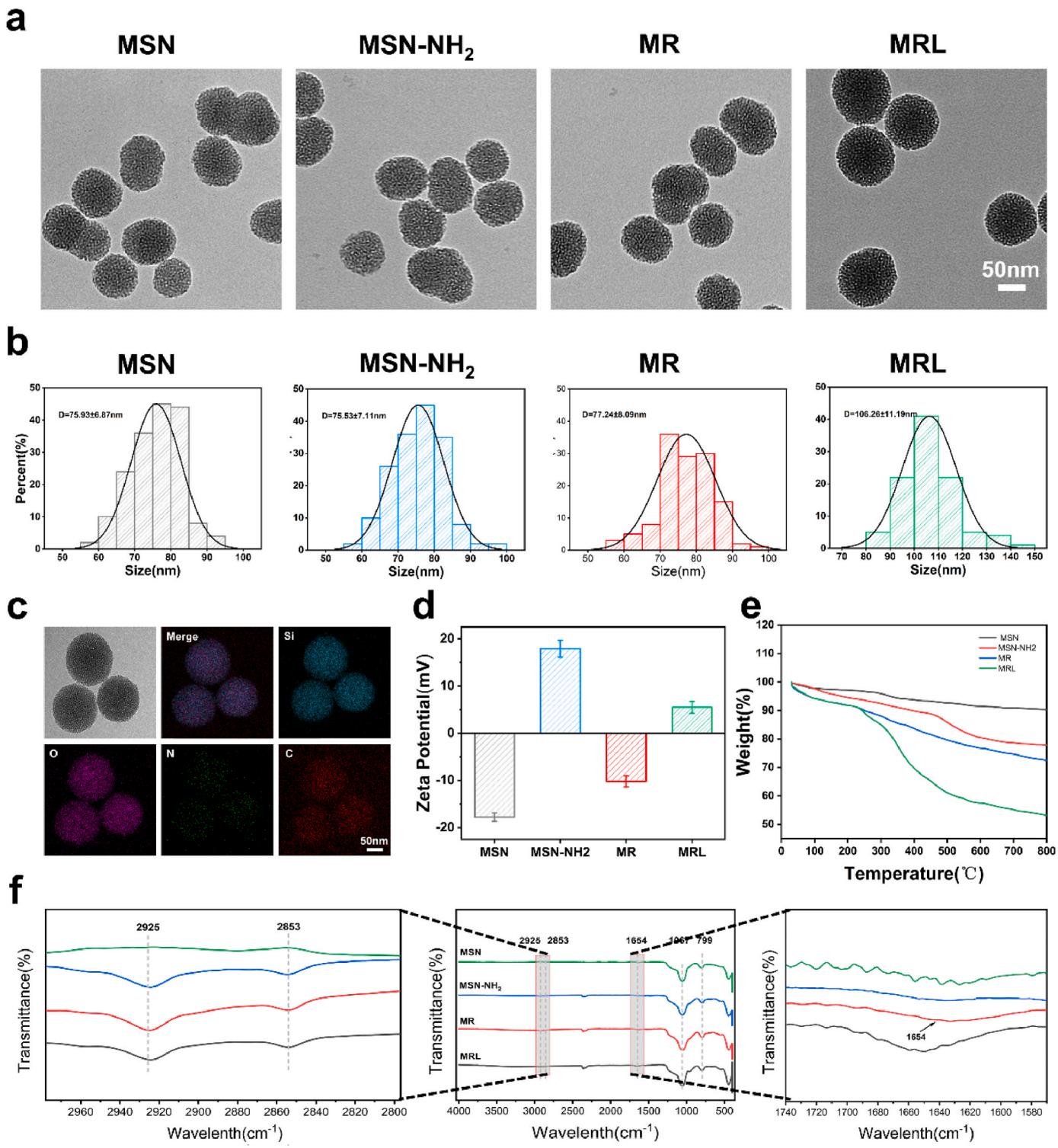

Fig. 1. Synthesis and characterization of MRL. a) Representative transmission electron microscopy (TEM) images of MSN, MSN-NH_2, MR, and MRL. Scale bar: 100 μm. b) Nanoparticles size distribution of MSN, MSN-NH_2, MR, and MRL. c) EDS elemental spectrum of the MRL. d) Zeta potential of MSN, MSN-NH_2, MR, and MRL nanoparticles. e) TGA curves of MSN, MSN-NH_2, MR, and MRL. f) FT-IR spectra of MSN, MSN-NH_2, MR, and MRL nanoparticles, with an enlarged view of characteristic peaks in the local region.

LL-37 to remain active in vivo for an extended period, thereby prolonging its half-life and reducing the required dosage.

In further elemental mapping analysis (Fig. 1c), silicon (Si), oxygen (O), nitrogen (N), and carbon (C) were observed to be uniformly distributed across the MRL nanoparticles, confirming the successful modification of MSNs-NH_2 with RGD and LL-37. Zeta potential testing revealed that the MSNs had a zeta potential of −17.8 mV, which was attributed to the abundance of Si-OH groups on the surface, indicating high polarity (Fig. 1d). After amino functionalization of the MSNs with APTES, the zeta potential of the MSNs-NH_2 increased to +17.9 mV, due to the positive charge resulting from amine protonation. Following RGD grafting, the zeta potential of MR decreased to −10.2 mV, likely due to

the deprotonation of -COOH groups in RGD, further confirming the successful modification of MSNs with RGD. Notably, after further loading of LL-37, the zeta potential of MRL shifted to a positive value (+5.5 mV), indicating the successful binding of positively charged LL-37 to MR. This finding also suggests that the negatively charged MR may facilitate LL-37 binding through electrostatic attraction. Thermogravimetric analysis (TGA) was employed to further analyze the composition of the MRL. As shown in Fig. 1e, the initial weight loss of the MSNs at approximately 100 °C was attributed primarily to the evaporation of adsorbed water. For MSNs-NH_2, weight loss in the 240–700 °C range was associated with the decomposition of aminopropyl groups. For MR, weight loss in the same temperature range was attributed to the degradation of RGD. The weight loss of MRL was greater than that of MR, particularly at 400 °C, which was attributed to the degradation of LL-37. Fourier transform-infrared (FT-IR) spectroscopy was employed to verify the successful modification and preparation of the composite material (Fig. 1f). The characteristic peak at 1067 cm^{-1} corresponded to the stretching vibration of O-Si-O in MSNs, and the peak at 799 cm^{-1} corresponded to the symmetric stretching vibration of Si-OH. For MSNs-NH_2, the peaks observed at 2925 cm^{-1} and 2853 cm^{-1} were attributed to C–H stretching vibrations resulting from the amine functionalization of the MSN surface. The peak at 1654 cm^{-1}, which was absent in the spectra of the MSNs and MSNs-NH_2 but was observed in the MR and MRL spectra, was attributed to -NH bending and -CN amide stretching, further confirming the successful formation of amide bonds. Additionally, a slight shift in the 1654 cm^{-1} peak corresponding to amide bond bending vibrations was observed in the FT-IR spectrum of MRL compared with MR, possibly due to interactions between LL-37 and MR. Finally, the loading efficiency and release properties of LL-37 were investigated. The BCA method was employed to measure the concentration of LL-37 in solution, and the encapsulation rate and drug loading rate were calculated as 24 ± 1.47 % and 19.95 ± 0.94 %, respectively, based on the change in LL-37 concentration before and after loading. To ensure consistency across groups, subsequent experiments were designed on the basis of equivalent drug-loading rates for all experimental groups. Additionally, LL-37 release was calculated by measuring changes in its concentration in the supernatant. The release profile shown in Fig. S2 (Supporting Information) indicates rapid release within the first 24 h, followed by a slow and sustained release trend, reaching a cumulative release of 78.37 % at 72 h.

To evaluate the biocompatibility of MRL, a CCK-8 assay was conducted to assess the effects of MR, LL-37, and MRL on cell viability. Fig. S3 (Supporting Information) and Fig. S5 (Supporting Information) demonstrate that both L929 cells and BMDMs exhibited good viability when co-incubated with MR and MRL at concentrations up to 256 μg mL^{-1}. However, compared to L929 cells, LL-37 exhibited greater toxicity toward BMDMs at the same concentration, likely due to its effect on inducing pyroptosis of BMDMs (Fig. S4, Supporting Information). Furthermore, no significant hemolysis was observed for MR or MRL, both of which exhibited strong hemocompatibility at concentrations up to 512 μg mL^{-1}. Even for LL-37, only mild hemolysis was observed at concentrations as high as 256 μg mL^{-1} (Fig. S6, Supporting Information). Therefore, 256 μg mL^{-1} was selected as the optimal concentration for subsequent immunomodulation and antimicrobial experiments.

In summary, the MRL demonstrated excellent biosafety, superior dispersibility, stable and uniform spherical structures, large specific surface area, and pore volume, as well as outstanding sustained release properties. These properties enable MRL to efficiently penetrate dense biofilm matrices and achieve a uniform distribution across different regions of the biofilm. Even at low concentrations, MRL exhibited exceptional biological effects, providing a robust foundation for its synergistic immunomodulatory and biofilm clearance capabilities.

2.2. Bactericidal and anti-biofilm activities of MRL

Traditional antibiotics for the treatment of IRIs are often limited by resistance and serious adverse effects, which pose significant challenges for the effective clearance of the infection. To evaluate the antibacterial efficacy of MRL, methicillin-resistant *Staphylococcus aureus* (MRSA) and *Escherichia coli* (*E. coli*) were selected as representative pathogens of IRIs for in vitro experiments.

We first assessed the bactericidal kinetics of MRL by co-culturing bacteria with MR, LL-37, or MRL, measuring the optical density of the bacterial suspensions at specific time points, and then plotted the growth curves (Fig. S7, Supporting Information). The results showed that the growth and proliferation of MRSA and *E. coli* were significantly inhibited after treatment with LL-37 and MRL, whereas the MR group exhibited little to no inhibitory effect. To further verify the effects of MRL on planktonic bacteria, MRSA and *E. coli* co-incubated with nanoparticles were transferred onto agar plates for continued cultivation, and bacterial survival rates were quantified (Fig. 2a–c). In contrast, no significant difference (ns) was detected between the MR group and the control group, indicating that MR alone had limited inhibitory effects on bacterial survival, whereas LL-37 and MRL exhibited significant bactericidal activity.

To investigate the anti-biofilm effects of MRL, we evaluated biofilm inhibition in different treatment groups via crystal violet staining (Fig. 2d–f). The results revealed that the biofilms of MRSA and *E. coli* in the control group exhibited uniform and dense purple staining, indicating the successful formation of stable biofilms in vitro for both bacteria. The biofilm density in the MR group was comparable to that in the control group, suggesting that MR alone had no significant anti-biofilm effect. However, in the LL-37 and MRL treatment groups, biofilm staining was significantly reduced. In particular, for *E. coli*, the staining became lighter and showed noticeable unevenness, indicating disruption of the biofilm structure. To directly observe the disruption of biofilms, bacterial biofilms were examined via confocal laser scanning microscopy (CLSM) and scanning electron microscopy (SEM) (Fig. 2g; Fig. S8, Supporting Information). The results showed that in the control and MR groups, the biofilm structures of MRSA and *E. coli* were compact and intact, exhibiting primarily green fluorescence. In contrast, in the LL-37 and MRL treatment groups, the biofilm structures became loose and fragmented, with abundant orange-red fluorescence, indicating that LL-37 and MRL had strong disruptive effects on the biofilms of MRSA and *E. coli*, significantly increasing bacterial mortality. To assess bacterial membrane integrity and damage, β-galactosidase activity was measured via an ONPG hydrolysis assay (Fig. 2h and i), which indirectly reflects bacterial metabolic function and cell membrane damage. The results revealed that OD_{420} values were low in the control and MR groups, indicating that bacterial cell membranes and metabolic functions were not significantly affected. In contrast, the LL-37 and MRL treatments significantly increased ONPG hydrolysis levels, with the highest degree of hydrolysis observed in the MRL group. These results demonstrate that MRL exerts antibacterial effects by disrupting the integrity of bacterial cell membranes. Additionally, protein leakage resulting from bacterial membrane disruption was quantified via the BCA method (Fig. S9, Supporting Information). The results revealed low protein leakage levels in the control and MR groups, whereas the LL-37 and MRL treatments significantly increased protein release, which was consistent with the results of the ONPG assay. Collectively, these findings demonstrate that MRL has exceptional potential in combating planktonic bacteria and biofilms, suggesting new research directions and therapeutic strategies for addressing IRIs-related infections.

2.3. Modulation of macrophage phenotypes by MRL

During the early stages of pathogen infection, macrophages play a crucial role in the immune response against pathogens [41]. Macrophages can exhibit two primary phenotypes, M1 and M2, depending on the conditions within the infection microenvironment (Fig. 3a) [42]. M1 macrophages are rapidly activated during the initial stages of infection and are characterized by the expression of the marker CD86 [43]. They

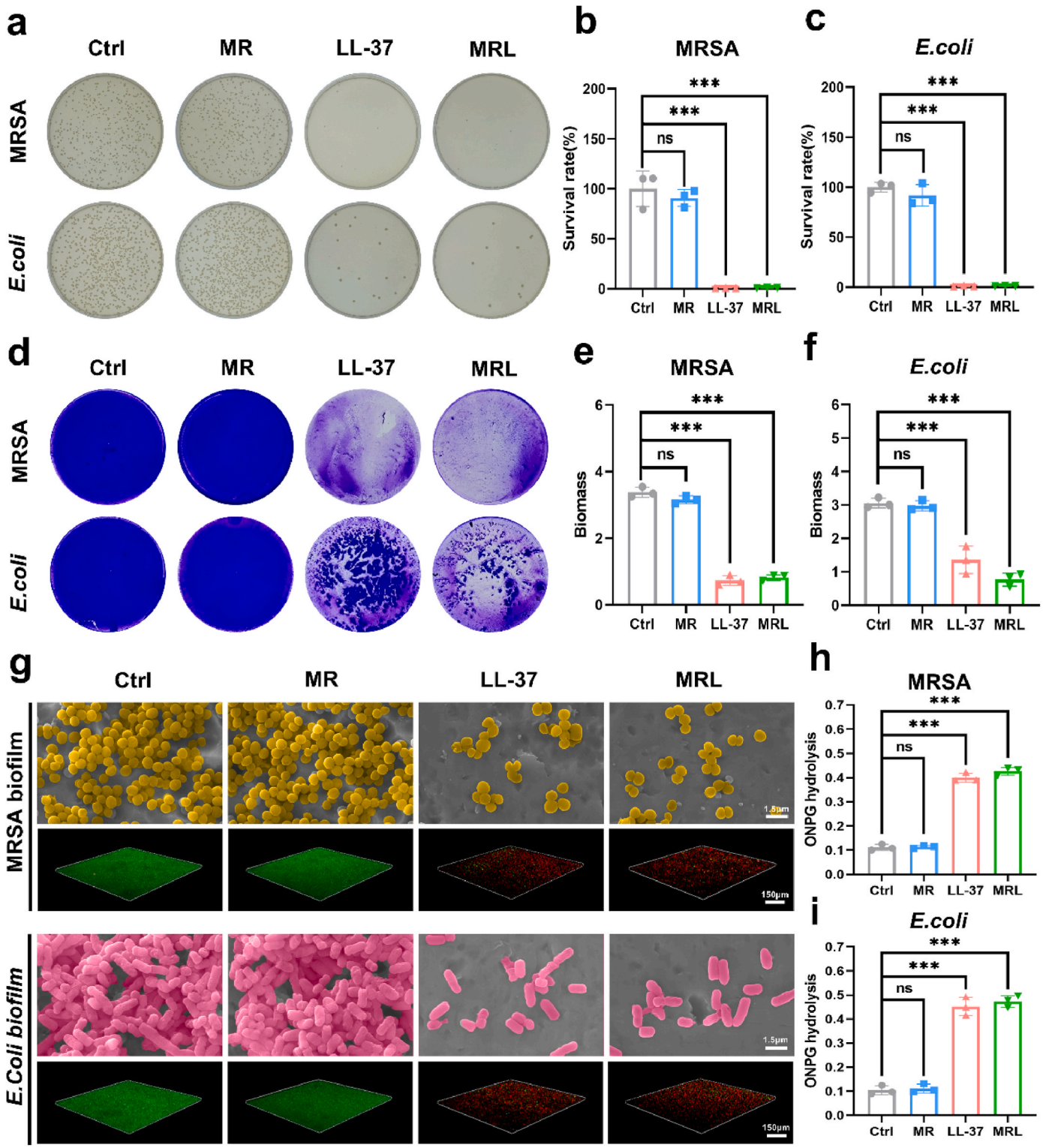

Fig. 2. Antibacterial properties of MRL. a) Representative images of SPM from MRSA and *E. coli* after incubation with different samples. b, c) Quantitative analysis corresponding to the SPM results (n = 3). d) Macro images illustrating the anti-biofilm effects on MRSA and *E. coli* biofilms on different substrates after crystal violet staining. Biofilm biomass of e) MRSA and f) *E. coli* after different treatments (n = 3). g) Representative SEM images of MRSA and *E. coli* biofilms, as well as representative CLSM 3D reconstruction images of MRSA and *E. coli* biofilms after bacterial viability/death (Syto9/PI) staining, scale bars = 1.5 μm (top) and 150 μm (bottom). h, i) Membrane permeability assessment of MRSA and *E. coli* treated with different conditions, measured by ONPG hydrolysis (n = 3). n represents the number of biologically independent experiments, and one-way ANOVA was used for statistical analysis. The data are presented as the means ± SD; ns means no significance, $p < 0.05$, $^{**}p < 0.01$, and $^{***}p < 0.001$.

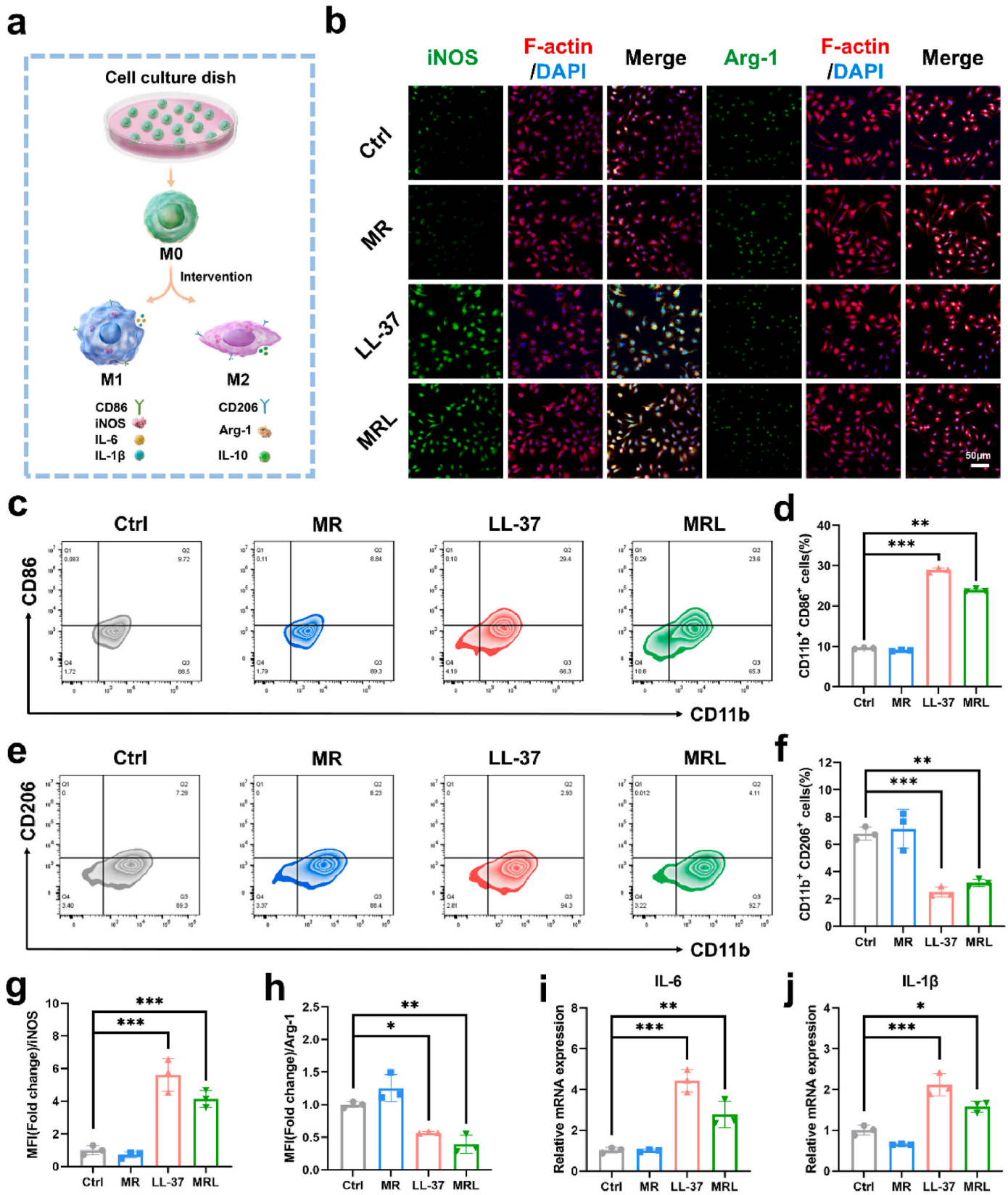

Fig. 3. MRL regulates macrophage polarization in vitro. a) The process of macrophage polarization. b) Representative CLSM images of macrophages cultured on different samples (green: iNOS or Arg-1; red: F-actin; blue: nucleus), scale bar = 50 μm. c-f) Flow cytometric analysis of CD86 (M1) and CD206 (M2) expression in macrophages cultured on different samples (n = 3). g, h) Quantification of the relative MFI from macrophage immunofluorescence staining (n = 3). i, j) RT−qPCR results of IL-6 and IL-1β expression (n = 3). n represents the number of biologically independent experiments, and one-way ANOVA was used for statistical analysis. The data are presented as the means ± SD, $p < 0.05$, $^{**}p < 0.01$, and $^{***}p < 0.001$.

rapidly bind to and engulf pathogens, forming phagosomes that digest the pathogens internally [44]. Additionally, they express inducible nitric oxide synthase (iNOS), creating a strong oxidative stress environment that disrupts the cell membranes, proteins, and nucleic acids of pathogens, leading to their direct destruction [45]. This phagocytic and degradative activity can rapidly inhibit pathogen proliferation during the early stages of infection. Additionally, M1 macrophages secrete large quantities of pro-inflammatory cytokines, such as IL-6 and IL-1β, which enhance local inflammatory responses and recruit neutrophils and other immune cells to the infection site, providing rapid immune support [46]. In contrast, M2 macrophages lack direct bactericidal activity and are characterized by the expression of the marker CD206 [47]. They express arginase-1 (Arg-1), which converts arginine into urea and ornithine, establishing a competitive relationship with iNOS to mitigate prolonged oxidative stress that could damage host tissues [48]. Furthermore, M2 macrophages secrete anti-inflammatory cytokines such as IL-10, which effectively suppressing the pro-inflammatory activity of M1 macrophages, preventing tissue damage caused by excessive inflammation, and contributing to anti-inflammatory and tissue repair functions [49].

M1 and M2 macrophages play opposing roles during the early stages of infection, and the balance between these phenotypes critically influences the efficacy of infection control [50]. In an optimal immune response, M1 macrophages dominate the early stages of infection, characterized by high expression of CD86 and iNOS, along with the secretion of cytokines such as IL-6 and IL-1β, to rapidly eliminate pathogens. However, in orthopedic implant-related infections, the extracellular polymeric substance (EPS) within biofilms hinders the M1 polarization of macrophages, resulting in an increased proportion of M2 macrophages. Excessive expression of Arg-1 and high secretion of IL-10 further suppress pro-inflammatory responses, leading to insufficient immune activation within the infection microenvironment. Consequently, pathogens evade immune surveillance, proliferate extensively, and spread, ultimately progressing into chronic infections.

Therefore, stimulating macrophages surrounding implants to polarize toward the M1 phenotype to promote infection clearance is a promising strategy. Hence, we further investigated the effects of MRL treatment on macrophage phenotype changes. Resting murine bone marrow-derived macrophages (BMDMs) were treated with different substrates, and their polarization status was assessed via immunofluorescence staining (Fig. 3b–g, h). In the control and MR groups, iNOS and Arg-1 expression levels were relatively low, indicating that BMDMs did not exhibit significant M1 or M2 polarization under basal conditions. In contrast, the LL-37 and MRL groups presented significantly greater mean fluorescence intensities of iNOS than the other groups did, indicating that LL-37 and MRL strongly induced M1 polarization of BMDMs and enhanced bactericidal and pro-inflammatory functions via high iNOS expression. Additionally, the LL-37 and MRL groups presented lower mean fluorescence intensities of Arg-1, further corroborating these findings. Flow cytometry was subsequently used to analyze the proportion of macrophages polarized toward the M1 phenotype. As shown in Fig. 3c and d, the proportion of $CD86^+$ cells increased from 9.6 % to 28.9 % and 23.9 % in the LL-37 and MRL groups, respectively, while the proportion of CD206+ cells decreased from 6.8 % to 2.5 % and 3.2 % (Fig. 3e and f), respectively. These results indicate that LL-37 and MRL significantly increase the proportion of M1 macrophages in BMDMs, thereby enabling the host to mount an effective immune response against implant-related infections. Additionally, the RT−qPCR results shown in Fig. 3i, j and Fig. S10 (Supporting Information) illustrate the capacity of macrophages to express pro-inflammatory cytokines (IL-6, IL-1β,iNOS and CD86) following intervention with different substrates. The results revealed that the IL-6 and IL-1β expression levels were significantly higher in the LL-37 and MRL treatment groups than in the other groups, indicating that the LL-37 and MRL treatments induced the secretion of large amounts of pro-inflammatory cytokines by macrophages, increasing proinflammatory responses and boosting local immune activity. These findings, which are consistent with previous immunofluorescence staining and flow cytometry results, further confirm that MRL has the potential to rapidly eliminate bacteria by stimulating BMDMs to transition to the M1 phenotype during the early stages of implant-related infections, thereby preventing rapid pathogen proliferation and spread, and effectively inhibiting biofilm formation.

2.4. The effect of MRL on macrophage pyroptosis

When the body is invaded by foreign pathogens, macrophages undergo moderate pyroptosis to help control early-stage infections. Pyroptosis is a form of programmed cell death characterized by the activation of inflammasomes (NLRP3) and the cleavage of Gasdermin D (GSDMD), which results in the formation of membrane pores to rapidly release pro-inflammatory cytokines such as IL-1β (Fig. 4a) [51]. Moderate pyroptosis not only directly eliminates pathogens but also enhances local antimicrobial effects by releasing pro-inflammatory cytokines that attract additional immune cells to the infection site [52].

However, in the biofilm microenvironment associated with implant-related infections, this process may be excessively activated, leading to a marked reduction in the number of macrophages and impairing their overall antimicrobial capacity. In biofilms, components such as lipopolysaccharides (LPS), lipoproteins, and peptidoglycans upregulate the NLRP3 expression in macrophages [53]. Subsequently, bacterial toxins and metabolic products within extracellular polymeric substances (EPS) induce potassium ion (K^+) efflux, further activating NLRP3 and causing its hyperactivation [54]. Activated NLRP3 recruits and activates caspase-1 (cysteine-aspartic acid protease 1), a key effector protein in the pyroptosis process. Caspase-1 then cleaves GSDMD, generating GSDMD-N fragments that insert into the cell membrane to form pores, leading to macrophage membrane rupture [55]. This results in the release of substantial intracellular contents, including IL-1β, causing extensive irreversible macrophage death, impairing collective immune activity, and allowing biofilm pathogens to evade immune attack, ultimately leading to recurrent and persistent infections around implants [56]. Furthermore, LL-37 released by MRL can further induce and exacerbate pyroptosis in macrophages within biofilms. Thus, regulating macrophage pyroptosis within the biofilm microenvironment to maintain a balanced state is critical for effectively treating implant-related infections. Therefore, we synthesized MRL nanoparticles through RGD modification to enhance macrophage viability, reduce cell death, and alleviate immunosuppression caused by excessive macrophage pyroptosis. We further investigated the role of MRL in regulating macrophage pyroptosis. Specific doses of LPS and Nigericin (a K^+ ionophore) were added to the macrophage culture medium to simulate the pyroptotic microenvironment of macrophages within biofilms in vitro [57].

We labeled macrophages with Annexin V-FITC and PI and then used flow cytometry to evaluate the effects of different treatments on macrophage pyroptosis (Fig. 4b; Fig. S11, Supporting Information). Compared with the control group, the LPS + Nig treatment increased the proportion of dead cells represented in the upper right quadrant (Q2) and lower right quadrant (Q3) of the flow cytometry plot from 9.57 % to 35.5 %, confirming that the LPS + Nig simulated biofilm microenvironment induces significant pyroptosis in macrophages. The addition of MR reduced the proportion of dead cells to 9.32 %, indicating that MR significantly inhibited macrophage pyroptosis and improved cell survival rates. Compared with the LPS + Nig group, the addition of LL-37 further increased the proportion of dead cells to 60.20 %, indicating that LL-37 exacerbated the pyroptosis effect induced by LPS + Nig, resulting in greater macrophage death. Following MR and MRL treatment, the proportion of dead cells decreased to 9.32 % and 25.50 %, respectively, further demonstrating the protective effects of our material on macrophages.

To explore the specific molecular mechanisms by which MRL regulates macrophage pyroptosis, we applied Western blotting to measure key pyroptosis-related proteins (Fig. 4c–g; Fig. S12, Supporting Information). The biofilm microenvironment simulated by the LPS + Nig

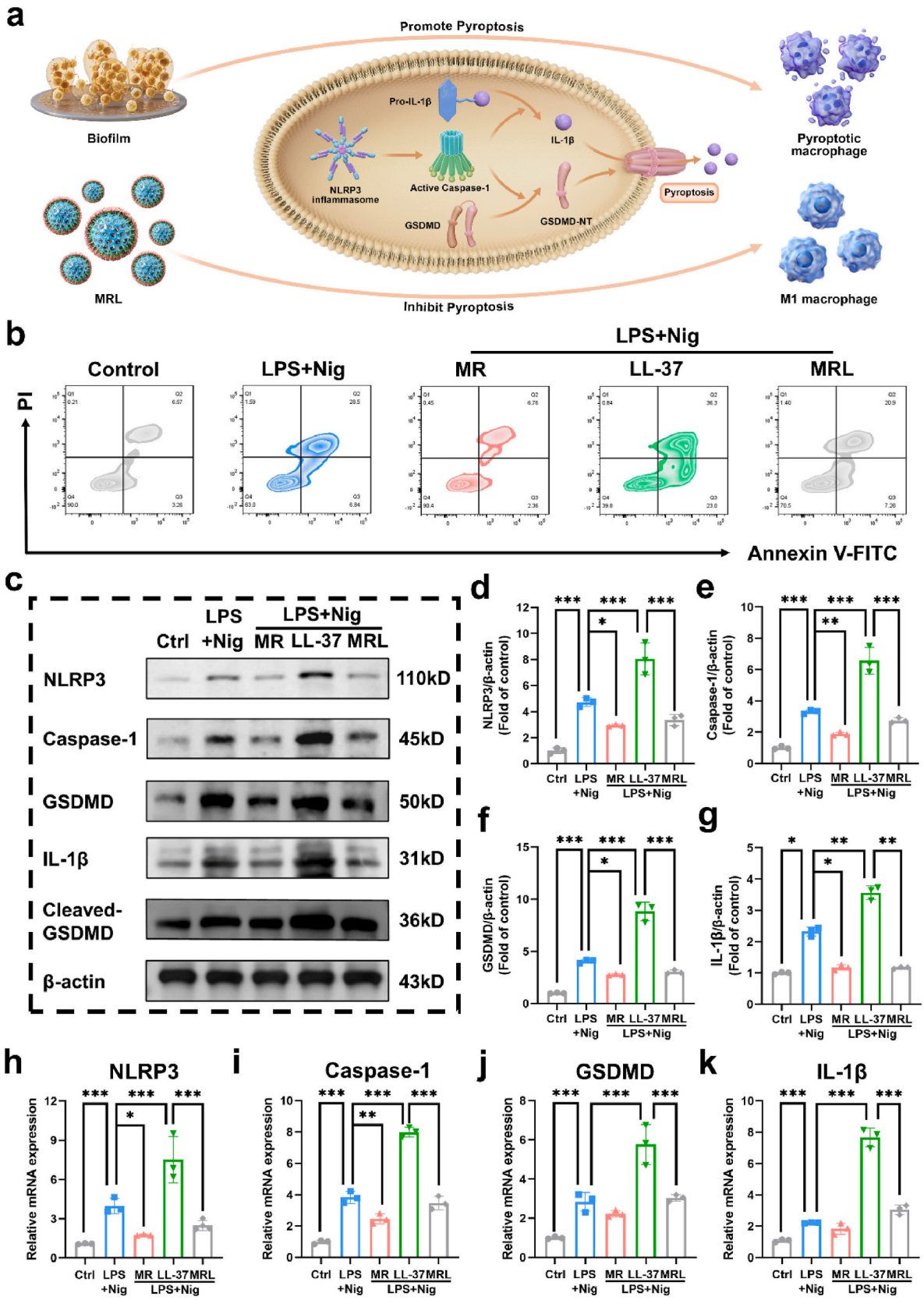

Fig. 4. Influence of MRL on the regulation of macrophage pyroptosis. a) Molecular mechanisms involved in the process of pyroptosis. b) Annexin V/PI staining was employed to identify and quantify cell death in macrophages following various treatments (n = 3). c) The relative protein expression levels of the pyroptosis-related proteins NLRP3, Caspase-1, GSDMD, IL-1β, and Cleaved-GSDMD were assessed via Western blotting. d-g) Quantification of the relative protein expression levels of NLRP3, Caspase-1, GSDMD, and IL-1β (n = 3). h-k) qRT−PCR was used to assess the relative expression levels of NLRP3, Caspase-1, GSDMD, and IL-1β in macrophages (n = 3). n represents the number of biologically independent experiments, and one-way ANOVA was used for statistical analysis. The data are presented as the means ± SD, $p < 0.05$, $^{**}p < 0.01$, and $^{***}p < 0.001$.

group significantly increased the expression of pyroptosis-associated proteins in macrophages, as evidenced by elevated levels of NLRP3, Caspase-1, GSDMD, IL-1β, and Cleaved-GSDMD. In contrast, MR and MRL suppressed the expression of these key proteins, indicating that RGD mitigates macrophage pyroptosis and preserves both macrophage functionality and population. We then measured the relative mRNA expression levels of NLRP3, Caspase-1, GSDMD, and IL-1β in macrophages via RT-qPCR, and the results were consistent with the protein expression levels (Fig. 4h–k).

Our study demonstrated that MRL can both promote macrophage polarization toward the M1 phenotype and inhibit excessive pyroptosis, thereby preserving macrophage populations and mitigating immune dysfunction caused by pyroptosis. Previous studies have shown that macrophages primarily eliminate infections through phagocytosing bacterial debris and necrotic tissue [58]. Therefore, we further investigated the changes in the antibacterial activity of macrophages following MRL treatment in vitro. The macrophages were co-cultured with MRSA and *E. coli* under various conditions. Surviving bacteria in the cell–bacteria co-culture system were quantified via the spread plate method (SPM) to evaluate the bactericidal capacity of the macrophages in each group. As shown in Fig. S13 (Supporting Information), the colony counts in the MR group, particularly in the MRL group, were significantly reduced, indicating that macrophages treated with MR and MRL effectively killed bacteria in the co-culture system. These results suggest that MR and MRL inhibited excessive macrophage pyroptosis, preserved viable macrophage populations, and enhanced their collective bactericidal capacity. Quantitative analysis revealed that after treatment with LPS + Nig + LL-37, the survival rate of MRSA was the highest, increasing from 100.00 % ± 11.08 % (control group) to 222.10 % ± 16.76 %, followed by the LPS + Nig group (195.1 % ± 21.95 %). In contrast, after treatment with MR and MRL, macrophage-mediated bacterial killing increased, resulting in a decrease in bacterial survival rates to 108.10 % ± 15.47 % and 93.82 % ± 17.62 %, respectively. Similar results were observed for *E. coli*. These findings demonstrate that MRL effectively enhances the phagocytic and bactericidal effects of macrophages.

2.5. In vivo effects of MRL on the inhibition of IRIs

To further validate the anti-biofilm efficacy of MRL in vivo and investigate its immunomodulatory mechanisms and potential effects on macrophage polarization and pyroptosis, additional studies were conducted. We established a subcutaneous implant infection model in mice, as shown in Fig. 5a, which illustrates the timeline from model establishment to treatment and evaluation. On day 0, titanium implants cultured with MRSA were inserted subcutaneously into the mice to induce implant-related infections. Treatment began on day 2 with MRL injections, followed by a second treatment on day 3 to reinforce efficacy. Histological analysis was performed on days 4 and 14 to assess the therapeutic outcomes.

Fig. 5b presents the wound healing process at the infection site on the backs of the mice across different treatment groups from day 0 to day 14. Throughout the observation period, the wounds in the control group exhibited persistent infection and deterioration. By day 4, noticeable purulent discharge and tissue ulceration were observed. By days 10 and 14, the wounds worsened further, with increased tissue necrosis and no signs of healing. In the MR group, wound healing was slightly better than that in the control group, but persistent purulent discharge and skin ulceration were still observed, and the healing process was relatively slow, indicating that MR had limited efficacy in suppressing infection progression. Compared with the control group, the wounds in the LL-37 treatment group began to show scabbing and mild signs of healing by day 4, with reduced infection severity. The wound area subsequently decreased slightly, but redness and swelling persisted, indicating ongoing inflammation. The MRL group exhibited the most significant anti-infective and healing effects. By day 7, the wounds were mostly dry with no apparent purulent discharge, demonstrating effective infection control. By day 10, the wound area continued to decrease with good tissue repair, and by day 14, the wounds had nearly healed completely. Fig. 5c shows changes in body weight over time in the different treatment groups, which were monitored from day 0 to day 14. The MRL treatment group showed sustained weight gain throughout the observation period, indirectly reflecting the superior anti-infective and healing effects of MRL in vivo, which significantly improved the overall health of the mice.

To further evaluate the bacterial load in the mice after treatment, we quantified the bacterial survival rates of the implants and surrounding tissues in the different groups via SPM (Fig. 5g–h; Fig. S15, Supporting Information). The culture plates of the control group presented abundant bacterial colonies. In contrast, in the MR and LL-37 groups, the bacterial survival rates on the implants decreased to 33.49 % and 23.47 %, respectively, while in the surrounding tissues, they decreased to 35.34 % and 35.20 %, respectively. These results indicate that both MR and LL-37 exhibit certain antibacterial effects in vivo, with the antibacterial efficacy of MR possibly linked to its ability to inhibit biofilm-induced macrophage pyroptosis. In the MRL group, the bacterial survival rates of the implants and surrounding tissues were reduced to 3.68 % and 1.98 %, respectively, demonstrating superior antibacterial effects. These results were further confirmed by SEM images of the implant surface. As shown in Fig. 5e, the implant surface in the control group was covered with abundant bacteria, which strongly aggregated and cross-linked, forming a thick biofilm structure. In the MR and LL-37 groups, the bacterial count was reduced, but significant bacterial attachment and noticeable biofilm structures remained. In contrast, the implant surface in the MRL group exhibited extensive fibroblast proliferation, with minimal bacterial attachment and almost complete disappearance of the biofilm, demonstrating significant inhibition of bacterial adhesion and biofilm formation. We further observed bacterial infections in the surrounding tissues of the implants via Giemsa staining (Fig. 5f). Yellow arrows indicate visible bacterial locations. In the control group, numerous bacteria were densely distributed in the tissue gaps, causing severe structural damage to the tissue. The MR and LL-37 groups showed a certain degree of antibacterial effects, but multiple bacterial aggregation regions remained in the tissues. Compared with those in the control group, bacteria were still concentrated in certain areas, indicating that MR and LL-37 exhibited relatively limited antibacterial activity in vivo and that local pathogens were not fully eradicated. In contrast, the MRL group demonstrated better anti-infective ability than the other groups did, with almost no visible bacterial infiltration and more intact tissue structures. These findings indicate that MRL treatment effectively inhibited bacterial infiltration in surrounding tissues, achieving significant infection control and preserving the health of the surrounding tissue.

To further illustrate infection and overall control of inflammation in the different treatment groups, we performed hematoxylin and eosin (H&E) staining on the tissues surrounding the implants (Fig. 5d; Fig. S16, Supporting Information). The tissue sections from the control group presented disorganized tissue structures, significant neutrophil infiltration, and inflammatory cell aggregation, reflecting persistent infection and chronic inflammation around the implants, which led to tissue damage. In the MR and LL-37 groups, the inflammatory response was reduced compared to that in the control group, but inflammatory cell aggregation and neutrophil infiltration were still observed, with limited tissue repair, indicating that MR had some inhibitory effects on infection and inflammation but was insufficient to completely eliminate the infection. In the MRL group, the tissue sections showed only sporadic inflammatory cell infiltration, with nearly complete resolution of the inflammatory response and more intact tissue structures, demonstrating optimal infection control and tissue repair outcomes.

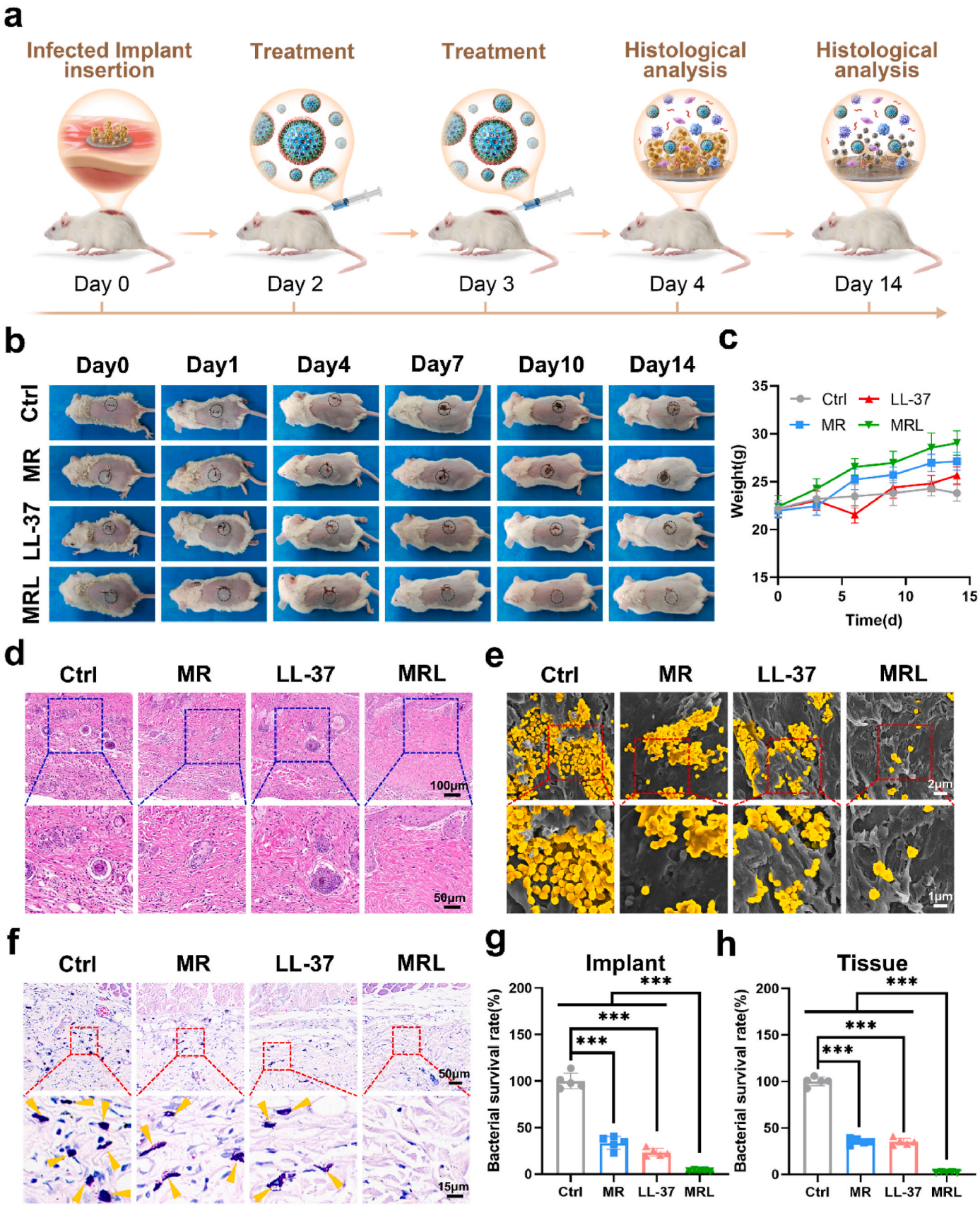

(caption on next page)

Fig. 5. The antibacterial properties of MRL in a mouse model of subcutaneous implant infection. a) Titanium plates co-cultured with MRSA were implanted subcutaneously in mice, and the in vivo experimental protocol was implemented. b) Representative macroscopic images of infected mice following various treatments. c) Changes in the body weights of the mice following different treatments (n = 5). d) Representative H&E-stained images of surrounding tissue around the implant on day 14, scale bars = 1.5 μm (top) and 150 μm (bottom). e) Representative SEM images of subcutaneous implants on day 14, scale bars = 1.5 μm (top) and 150 μm (bottom). f) Representative Giemsa-stained images of surrounding tissue around the implant on day 14, scale bars = 1.5 μm (top) and 150 μm (bottom). g) Quantitative analysis of bacterial colonies corresponding to the implant (n = 5). h) Quantitative analysis of bacterial colonies corresponding to surrounding tissue (n = 5). n represents the number of biologically independent experiments, and one-way ANOVA was used for statistical analysis. The data are presented as the means ± SD, $p < 0.05$, $^{**}p < 0.01$, and $^{***}p < 0.001$.

2.6. The coordinated regulation of macrophage polarization and pyroptosis by MRL in vivo

We further investigated the process by which MRL regulates macrophage polarization and pyroptosis in vivo. As shown in Fig. 6a and Fig. S17 (Supporting Information), in the control group, biofilms significantly inhibited macrophage polarization toward the M1 phenotype, leading to low iNOS expression that failed to reach effective

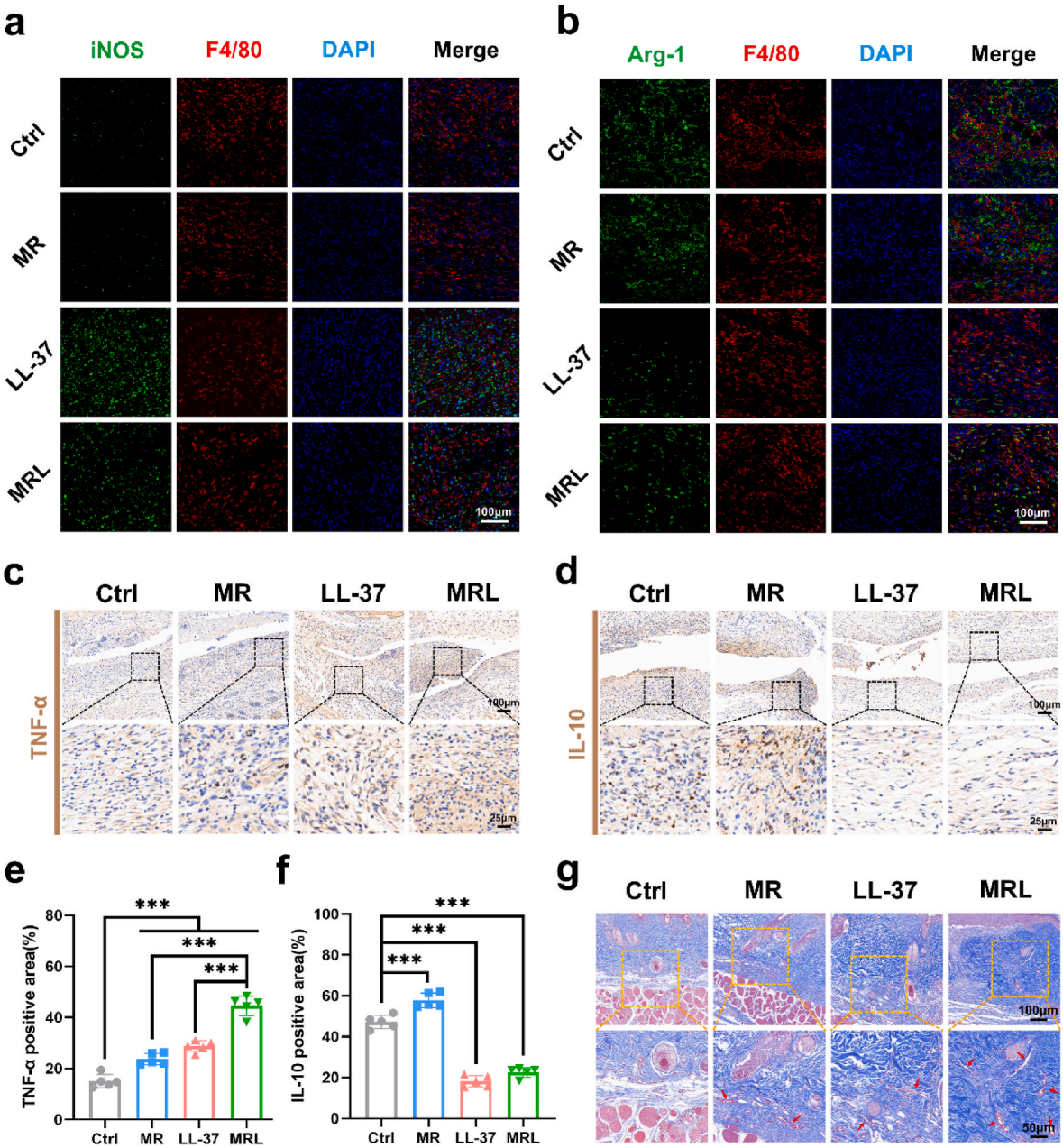

Fig. 6. Coordinated regulation of macrophage polarization and pyroptosis by MRL in vivo. a, b) Representative immunofluorescence images of surrounding tissue around the implant: green (M1 marker, iNOS; or M2 marker, Arg-1), red (F4/80, mouse macrophage antigen), and blue (nuclei), scale bar = 100 μm. c, d) Representative immunohistochemical images of TNF-α and IL-10 in the surrounding tissue around the implant, scale bars = 100 μm (top) and 25 μm (bottom). e, f) Quantification of TNF-α and IL-10 positive area (n = 5). g) Representative Masson staining images of skin tissue on day 14 in the subcutaneous implant infection model, scale bars = 100 μm (top) and 50 μm (bottom). n represents the number of biologically independent experiments, and one-way ANOVA was used for statistical analysis. The data are presented as the means ± SD, $p < 0.05$, $^{**}p < 0.01$, and $^{***}p < 0.001$.

antibacterial levels, which is a key factor in the host's inability to control the infection. In the LL-37 group, the mean fluorescence intensity of iNOS was higher, with a noticeable increase in M1 macrophages, indicating that LL-37 significantly induced macrophage polarization toward the M1 phenotype and activated the host's antibacterial immune response. In the MRL group, the mean fluorescence intensity of iNOS was slightly lower than that in the LL-37 group, but the number of macrophages increased, suggesting that MRL strongly promoted macrophage polarization toward the M1 phenotype while suppressing excessive pyroptosis, thereby significantly enhancing the bactericidal effect of macrophages. Compared to the control group, the mean fluorescence intensity of Arg-1 was lower in both the LL-37 and MRL groups, indicating that LL-37 and MRL inhibited macrophage polarization toward the anti-inflammatory M2 phenotype to some extent (Fig. 6b; Fig. S18, Supporting Information), thereby enhancing early bactericidal effects and further supporting the ability of MRL to regulate macrophages and enhance host immune activity.

As shown in Figs. S19 and S20 (Supporting Information), different treatments influence Gasdermin D (GSDMD) expression in macrophages within the tissue surrounding the implants. GSDMD is a key effector protein in the pyroptosis pathway that is capable of inserting into cell membranes to form pores, triggering pyroptosis and the release of pro-inflammatory cytokines. In the control group, the green fluorescence signal of GSDMD was relatively high, indicating that biofilms surrounding the infected implant upregulated GSDMD expression through inflammasome activation, thereby inducing macrophage pyroptosis. However, as shown in Fig. S15 (Supporting Information), the control group did not effectively control the infection, likely because excessive pyroptosis induced extensive macrophage death, significantly reducing the number of macrophages around the infected area. Although pyroptosis can help the host limit infections and clear bacteria, it cannot fully compensate for the loss of immune activity caused by the substantial reduction in macrophage populations. In the MR group, the fluorescence signal of GSDMD was weaker than in the control group, indicating that MR effectively inhibited macrophage pyroptosis and preserved macrophage immune activity. In the LL-37 group, the green fluorescence signal of GSDMD was the strongest, suggesting that LL-37 exacerbated macrophage pyroptosis in vivo, which was consistent with our in vitro results. Compared to the control and LL-37 groups, the fluorescence signal of GSDMD in the MRL group was significantly lower, approaching that in the MR group. These findings suggest that MRL effectively optimized the pyroptosis process in vivo through RGD modification, significantly reducing GSDMD expression, which further explains why MRL was more effective than LL-37 at controlling implant-related infections (Fig. S15, Supporting Information). In the MRL group, macrophage pyroptosis was maintained at an optimal balance, ensuring effective infection clearance while avoiding immune dysfunction caused by excessive pyroptosis.

The immunohistochemical analysis shown in Fig. 6c–f indicate that under implant-associated infection conditions, TNF-α expression levels were low in the control group. This may be due to the biofilm surrounding the implant infection both inhibiting macrophage polarization toward the M1 phenotype and inducing pyroptosis, thereby reducing macrophage populations and resulting in insufficient TNF-α secretion. Moreover, IL-10 expression was higher in the control group, further confirming that biofilms inhibited macrophage polarization toward the M1 phenotype while promoting polarization toward the M2 phenotype. In the MR group, TNF-α expression was higher than that in the control group, likely because the RGD in the MR suppressed excessive macrophage pyroptosis, which increased the total macrophage population and indirectly increased TNF-α expression levels. However, since LL-37 exacerbated macrophage pyroptosis, reducing the total number of macrophages, the TNF-α expression levels in the LL-37 group were lower than those in the MRL group. MRL not only significantly inhibited macrophage polarization toward the M2 phenotype by reducing IL-10 expression levels but also effectively suppressed macrophage pyroptosis through RGD modulation, ensuring adequate antibacterial capacity around the biofilm.

To further evaluate the therapeutic effects of each group and assess the extent of tissue repair and regeneration after infection, we used Masson staining to visualize the collagen distribution and content in the tissues surrounding the implants (Fig. 6g; Fig. S21, Supporting Information). In the control group, persistent infection and uncontrolled inflammation limited tissue repair, resulting in the least collagen deposition. Although LL-37 exhibits certain antibacterial and pro-inflammatory effects, excessive pyroptosis impairs its antibacterial efficacy and limits further collagen deposition. MRL enhances macrophage immune activity while suppressing excessive pyroptosis, preserving the number and function of macrophages, improving the local immune microenvironment, significantly increasing collagen deposition, and promoting tissue repair and regeneration. Additionally, H&E staining of major organs (heart, liver, spleen, lungs, and kidneys) revealed no apparent toxicity, indicating that MRL exhibits excellent biocompatibility in vivo (Fig. S22, Supporting Information).

3. Conclusion

In this study, a mesoporous silica nanoparticle system, MRL, modified with the RGD tripeptide and adsorbed with the antimicrobial peptide LL-37, was developed on the basis of an immunomodulatory strategy to coordinate the regulation of macrophage pyroptosis and polarization for the effective treatment of IRIs. Compared to traditional antibiotics, MRL overcomes the limitations of adverse reactions and antibiotic resistance due to its excellent sustained-release properties and highly conserved antimicrobial mechanism. Both in vitro and in vivo experiments demonstrated the superior antibacterial and anti-biofilm activities of MRL. Additionally, MRL coordinates the regulation of macrophage pyroptosis and polarization, preserves the collective immune activity of macrophages, alleviates the immunosuppressive effects of biofilms on macrophages, and rapidly, efficiently, and comprehensively eliminates IRIs. This study is the first to combine RGD modification with an LL-37 nanodelivery system. It proposes a targeted strategy to regulate macrophage pyroptosis, a key pathological mechanism in biofilm infections. This approach may offer new insights for treating IRIs and promote the clinical application of anti-biofilm nanomaterials.

Although the initial results are promising, further optimization of MRL is needed. In future research, our primary focus will be on improving the physicochemical properties of MRL nanoparticles to enhance their targeting capacity and biofilm penetration. Furthermore, we will explore the combined use of MRL with other antimicrobial agents or therapeutic strategies to amplify its therapeutic efficacy. We hope these efforts will contribute to advancing the clinical application of the MRL system and provide more effective treatment options for IRIs.

CRediT authorship contribution statement

Zhi Li: Writing – original draft, Software, Project administration, Methodology. **Yuhang Wang:** Investigation, Data curation, Conceptualization. **Xingshi Yuan:** Supervision, Software, Investigation, Data curation. **Mingyou Xu:** Visualization, Validation, Supervision. **Xiaofang Wang:** Software. **Chang Liu:** Software. **Chen Zhu:** Writing – review & editing, Conceptualization. **Wei Pei:** Writing – review & editing, Data curation, Conceptualization. **Jiaxiang Bai:** Writing – review & editing, Funding acquisition, Data curation, Conceptualization. **Xifu Shang:** Writing – review & editing, Supervision, Project administration, Funding acquisition, Conceptualization.

Declaration of competing interest

The authors declare that they have no known competing financial interests or personal relationships that could have appeared to influence the work reported in this paper.

Acknowledgments

This work was supported by the National Natural Science Foundation of China (No. 82402780, 82102478, 82072408), China; China National Postdoctoral Program for Innovative Talents (No. BX20230350), China; Research Funds of Centre for Leading Medicine and Advanced Technologies of IHM (No. 2023IHM02007, 2023IHM01075), China; Natural Science Foundation of Anhui Province (No. 2308085MH251), China; Joint Fund for Medical Artificial Intelligence (No. MAI2023Q027), China;China Postdoctoral Science Foundation (No. 2024M753130), China.

Appendix A. Supplementary data

Supplementary data to this article can be found online at https://doi.org/10.1016/j.mtbio.2025.101629.

Data availability

Data will be made available on request.

References

[1] M. Roudbary, R. Vahedi-Shahandashti, A. Santos, S. Roudbar Mohammadi, P. Aslani, C. Lass-Flörl, C.F. Rodrigues, Biofilm formation in clinically relevant filamentous fungi: a therapeutic challenge, Crit. Rev. Microbiol. 48 (2022) 197–221, https://doi.org/10.1080/1040841x.2021.1950121.

[2] Y. Li, Y. Dong, Z. Zhang, Z.T. Lin, C. Liang, M.X. Wu, Efficient photolysis of multidrug-resistant polymicrobial biofilms, Adv. Sci. (2024) e2407898, https://doi.org/10.1002/advs.202407898.

[3] Y. Hu, S. Li, H. Dong, L. Weng, L. Yuwen, Y. Xie, J. Yang, J. Shao, X. Song, D. Yang, L. Wang, Environment-responsive therapeutic platforms for the treatment of implant infection, Adv Healthc Mater 12 (2023) e2300985, https://doi.org/10.1002/adhm.202300985.

[4] S. Das, T.W. Kaminski, B.T. Schlegel, W. Bain, S. Hu, A. Patel, S.L. Kale, K. Chen, J. S. Lee, R.K. Mallampalli, V.E. Kagan, D. Rajasundaram, B.J. McVerry, P. Sundd, G. D. Kitsios, A. Ray, P. Ray, Neutrophils and galectin-3 defend mice from lethal bacterial infection and humans from acute respiratory failure, Nat. Commun. 15 (2024) 4724, https://doi.org/10.1038/s41467-024-48796-y.

[5] A. Sabnis, K.L. Hagart, A. Klöckner, M. Becce, L.E. Evans, R.C.D. Furniss, D. A. Mavridou, R. Murphy, M.M. Stevens, J.C. Davies, G.J. Larrouy-Maumus, T. B. Clarke, A.M. Edwards, Colistin kills bacteria by targeting lipopolysaccharide in the cytoplasmic membrane, Elife 10 (2021), https://doi.org/10.7554/eLife.65836.

[6] M.A. Cook, G.D. Wright, The past, present, and future of antibiotics, Sci. Transl. Med. 14 (2022) eabo7793, https://doi.org/10.1126/scitranslmed.abo7793.

[7] S. Zhang, B. Yu, C. Sheng, C. Yao, Y. Liu, J. Wang, Q. Zeng, Y. Mao, J. Bei, B. Zhu, S. Chen, SHISA3 reprograms tumor-associated macrophages toward an antitumoral phenotype and enhances cancer immunotherapy, Adv. Sci. 11 (2024) e2403019, https://doi.org/10.1002/advs.202403019.

[8] X. Xian, L.L. Cai, Y. Li, R.C. Wang, Y.H. Xu, Y.J. Chen, Y.H. Xie, X.L. Zhu, Y.F. Li, Neuron secrete exosomes containing miR-9-5p to promote polarization of M1 microglia in depression, J. Nanobiotechnol. 20 (2022) 122, https://doi.org/10.1186/s12951-022-01332-w.

[9] H. Ruan, A. Aulova, V. Ghai, S. Pandit, M. Lovmar, I. Mijakovic, R. Kádár, Polysaccharide-based antibacterial coating technologies, Acta Biomater. 168 (2023) 42–77, https://doi.org/10.1016/j.actbio.2023.07.023.

[10] X. Ji, X. Huang, C. Li, N. Guan, T. Pan, J. Dong, L. Li, Effect of tumor-associated macrophages on the pyroptosis of breast cancer tumor cells, Cell Commun. Signal. 21 (2023) 197, https://doi.org/10.1186/s12964-023-01208-y.

[11] Q. Chai, S. Yu, Y. Zhong, Z. Lu, C. Qiu, Y. Yu, X. Zhang, Y. Zhang, Z. Lei, L. Qiang, B.X. Li, Y. Pang, X.B. Qiu, J. Wang, C.H. Liu, A bacterial phospholipid phosphatase inhibits host pyroptosis by hijacking ubiquitin, Science (New York, N.Y.) 378 (2022) eabq0132, https://doi.org/10.1126/science.abq0132.

[12] Y. Zhang, Y. Cheng, Z. Zhao, S. Jiang, Y. Zhang, J. Li, S. Huang, W. Wang, Y. Xue, A. Li, Z. Tao, Z. Wu, X. Zhang, Enhanced chemoradiotherapy for MRSA-infected osteomyelitis using immunomodulatory polymer-reinforced nanotherapeutics, Adv Mater 36 (2024) e2304991, https://doi.org/10.1002/adma.202304991.

[13] S. Artiaco, B. Limone, D. Vezza, F. Bosco, F. Giustra, G. Colzani, Treatment of infected soft tissue loss, Plastic and Aesthetic Research. http://doi.org/10.20517/2347-9264.2022.145, 2023.

[14] W. Li, Q. Chen, Y. Ma, H. Su, H. Ren, H. Wang, Antibacterial hydrogels for bacteria-infected wound treatment, Biomedical Technology 9 (2025), https://doi.org/10.1016/j.bmt.2024.11.001.

[15] L. de Vor, B. van Dijk, K. van Kessel, J.S. Kavanaugh, C. de Haas, P.C. Aerts, M. C. Viveen, E.C. Boel, A.C. Fluit, J.M. Kwiecinski, G.C. Krijger, R.M. Ramakers, F. J. Beekman, E. Dadachova, M.G. Lam, H.C. Vogely, B.C. van der Wal, J.A. van Strijp, A.R. Horswill, H. Weinans, S.H. Rooijakkers, Human monoclonal antibodies against Staphylococcus aureus surface antigens recognize in vitro and in vivo biofilm, Elife 11 (2022), https://doi.org/10.7554/eLife.67301.

[16] C. de la Fuente-Nunez, A. Cesaro, R.E.W. Hancock, Antibiotic failure: beyond antimicrobial resistance, Drug Resist. Updates : reviews and commentaries in antimicrobial and anticancer chemotherapy 71 (2023) 101012, https://doi.org/10.1016/j.drup.2023.101012.

[17] L. Wang, T. Tkhilaishvili, Z. Jiang, R.F. Pirlar, Y. Ning, A. Millán Laleona, J. Wang, J. Tang, Q. Wang, A. Trampuz, M. Gonzalez Moreno, X. Zhang, Phage-liposome nanoconjugates for orthopedic biofilm eradication, J Control Release 376 (2024) 949–960, https://doi.org/10.1016/j.jconrel.2024.09.049.

[18] Y. Rao, Y. Wang, H. Zhang, Y. Wang, Q. He, X. Yuan, J. Guo, H. Chen, A strategy of killing two birds with one stone for blocking drug resistance spread with engineered bdellovibrio bacteriovorus, Adv Mater 36 (2024) e2406910, https://doi.org/10.1002/adma.202406910.

[19] R. Yu, H. Chen, J. He, Z. Zhang, J. Zhou, Q. Zheng, Z. Fu, C. Lu, Z. Lin, F. Caruso, X. Zhang, Engineering antimicrobial metal-phenolic network nanoparticles with high biocompatibility for wound healing, Adv Mater 36 (2024) e2307680, https://doi.org/10.1002/adma.202307680.

[20] Y. Wang, C. Cao, Y. Zhu, H. Fan, Q. Liu, Y. Liu, K. Chen, Y. Wu, S. Liang, M. Li, L. Li, X. Liu, Y. Zhang, C. Wu, G. Lu, M. Wu, TREM2/β-catenin attenuates NLRP3 inflammasome-mediated macrophage pyroptosis to promote bacterial clearance of pyogenic bacteria, Cell Death Dis. 13 (2022) 771, https://doi.org/10.1038/s41419-022-05193-x.

[21] L. Wang, C. Zhang, J. Zhao, Z. Zhu, J. Wang, W. Fan, W. Jia, Biomimetic targeting nanoadjuvants for sonodynamic and chronological multi-immunotherapy against holistic biofilm-related infections, Adv Mater 36 (2024) e2308110, https://doi.org/10.1002/adma.202308110.

[22] R. Yao, Y. Chen, H. Hao, Z. Guo, X. Cheng, Y. Ma, Q. Ji, X. Yang, Y. Wang, X. Li, Z. Wang, Pathogenic effects of inhibition of mTORC1/STAT3 axis facilitates Staphylococcus aureus-induced pyroptosis in human macrophages, Cell Commun. Signal. 18 (2020) 187, https://doi.org/10.1186/s12964-020-00677-9.

[23] X. Zheng, W. Chen, F. Gong, Y. Chen, E. Chen, The role and mechanism of pyroptosis and potential therapeutic targets in sepsis: a review, Front. Immunol. 12 (2021) 711939, https://doi.org/10.3389/fimmu.2021.711939.

[24] T.D. Scherr, M.L. Hanke, O. Huang, D.B. James, A.R. Horswill, K.W. Bayles, P. D. Fey, V.J. Torres, T. Kielian, Staphylococcus aureus biofilms induce macrophage dysfunction through leukocidin AB and alpha-toxin, mBio 6 (2015), https://doi.org/10.1128/mBio.01021-15.

[25] Z. Rao, Y. Zhu, P. Yang, Z. Chen, Y. Xia, C. Qiao, W. Liu, H. Deng, J. Li, P. Ning, Z. Wang, Pyroptosis in inflammatory diseases and cancer, Theranostics 12 (2022) 4310–4329, https://doi.org/10.7150/thno.71086.

[26] R.A. Mustafa, P. Parkkila, J.M. Rosenholm, H. Zhang, T. Viitala, Monitoring silica core@shell nanoparticle-bacterial film interactions using the multi-parametric surface plasmon resonance technique, Smart Med. 2 (2023) e20230012, https://doi.org/10.1002/SMMD.20230012.

[27] D. Huang, L. Cai, N. Li, Y. Zhao, Ultrasound-trigged micro/nanorobots for biomedical applications, Smart Med 2 (2023) e20230003, https://doi.org/10.1002/SMMD.20230003.

[28] W. Xiu, X. Li, Q. Li, M. Ding, Y. Zhang, L. Wan, S. Wang, Y. Gao, Y. Mou, L. Wang, H. Dong, Ultrasound-stimulated "exocytosis" by cell-like microbubbles enhances antibacterial species penetration and immune activation against implant infection, Adv. Sci. 11 (2024) e2307048, https://doi.org/10.1002/advs.202307048.

[29] C.A. Roque-Borda, L. Primo, K.P. Medina-Alarcón, I.C. Campos, C.F. Nascimento, M.M.S. Saraiva, A. Berchieri Junior, A.M. Fusco-Almeida, M.J.S. Mendes-Giannini, J. Perdigão, F.R. Pavan, F. Albericio, Antimicrobial peptides: a promising alternative to conventional antimicrobials for combating polymicrobial biofilms, Adv. Sci. (2024) e2410893, https://doi.org/10.1002/advs.202410893.

[30] X. Kong, V. Vishwanath, P. Neelakantan, Z. Ye, Harnessing antimicrobial peptides in endodontics, Int. Endod. J. 57 (2024) 815–840, https://doi.org/10.1111/iej.14043.

[31] K.E. Ridyard, J. Overhage, The potential of human peptide LL-37 as an antimicrobial and anti-biofilm agent, Antibiotics (Basel, Switzerland) 10 (2021), https://doi.org/10.3390/antibiotics10060650.

[32] M. Jin, S. Liang, J. Wang, H. Zhang, Y. Zhang, W. Zhang, S. Liu, F. Xie, Endopeptidase O promotes Streptococcus suis immune evasion by cleaving the host- defence peptide cathelicidins, Virulence 14 (2023) 2283896, https://doi.org/10.1080/21505594.2023.2283896.

[33] A.M. van der Does, H. Beekhuizen, B. Ravensbergen, T. Vos, T.H. Ottenhoff, J. T. van Dissel, J.W. Drijfhout, P.S. Hiemstra, P.H. Nibbering, LL-37 directs macrophage differentiation toward macrophages with a proinflammatory signature, J. Immunol. 185 (2010) 1442–1449, https://doi.org/10.4049/jimmunol.1000376.

[34] S.H. Yoon, I. Hwang, E. Lee, H.J. Cho, J.H. Ryu, T.G. Kim, J.W. Yu, Antimicrobial peptide LL-37 drives rosacea-like skin inflammation in an NLRP3-dependent manner, J. Invest. Dermatol. 141 (2021) 2885–2894.e2885, https://doi.org/10.1016/j.jid.2021.02.745.

[35] B. Xu, S. Li, R. Shi, H. Liu, Multifunctional mesoporous silica nanoparticles for biomedical applications, Signal Transduct. Targeted Ther. 8 (2023) 435, https://doi.org/10.1038/s41392-023-01654-7.

[36] A. Lérida-Viso, A. Estepa-Fernández, A. García-Fernández, V. Martí-Centelles, R. Martínez-Máñez, Biosafety of mesoporous silica nanoparticles; towards clinical translation, Adv. Drug Deliv. Rev. 201 (2023) 115049, https://doi.org/10.1016/j.addr.2023.115049.

[37] H. Zhang, Z. Wang, H.T.T. Nguyen, A.J. Watson, Q. Lao, A. Li, J. Zhu, Integrin α(5)β(1) contributes to cell fusion and inflammation mediated by SARS-CoV-2 spike via RGD-independent interaction, Proc Natl Acad Sci U S A. 120 (2023) e2311913120, https://doi.org/10.1073/pnas.2311913120.

[38] D. Courter, H. Cao, S. Kwok, C. Kong, A. Banh, P. Kuo, D.M. Bouley, C. Vice, O. T. Brustugun, N.C. Denko, A.C. Koong, A. Giaccia, Q.T. Le, The RGD domain of human osteopontin promotes tumor growth and metastasis through activation of survival pathways, PLoS One 5 (2010) e9633, https://doi.org/10.1371/journal.pone.0009633.

[39] L.B. Gallagher, E.B. Dolan, J. O'Sullivan, R. Levey, B.L. Cavanagh, L. Kovarova, M. Pravda, V. Velebny, T. Farrell, F.J. O'Brien, G.P. Duffy, Pre-culture of mesenchymal stem cells within RGD-modified hyaluronic acid hydrogel improves their resilience to ischaemic conditions, Acta Biomater. 107 (2020) 78–90, https://doi.org/10.1016/j.actbio.2020.02.043.

[40] K. Braun, A. Pochert, M. Lindén, M. Davoudi, A. Schmidtchen, R. Nordström, M. Malmsten, Membrane interactions of mesoporous silica nanoparticles as carriers of antimicrobial peptides, J. Colloid Interface Sci. 475 (2016) 161–170, https://doi.org/10.1016/j.jcis.2016.05.002.

[41] A.V. Jäger, P. Arias, M.V. Tribulatti, M.A. Brocco, M.V. Pepe, A. Kierbel, The inflammatory response induced by Pseudomonas aeruginosa in macrophages enhances apoptotic cell removal, Sci. Rep. 11 (2021) 2393, https://doi.org/10.1038/s41598-021-81557-1.

[42] S. Kadomoto, K. Izumi, A. Mizokami, Macrophage polarity and disease control, Int. J. Mol. Sci. 23 (2021), https://doi.org/10.3390/ijms23010144.

[43] X. Dai, L. Lu, S. Deng, J. Meng, C. Wan, J. Huang, Y. Sun, Y. Hu, B. Wu, G. Wu, J. F. Lovell, H. Jin, K. Yang, USP7 targeting modulates anti-tumor immune response by reprogramming Tumor-associated Macrophages in Lung Cancer, Theranostics 10 (2020) 9332–9347, https://doi.org/10.7150/thno.47137.

[44] M. Zhao, N. Chen, Y. Guo, N. Wu, B. Cao, B. Zhan, Y. Li, T. Zhou, F. Zhu, C. Guo, Y. Shi, Q. Wang, Y. Li, L. Zhang, D-mannose acts as a V-ATPase inhibitor to suppress inflammatory cytokines generation and bacterial killing in macrophage, Mol. Immunol. 162 (2023) 84–94, https://doi.org/10.1016/j.molimm.2023.08.013.

[45] K.K. Wu, X. Xu, M. Wu, X. Li, M. Hoque, G.H.Y. Li, Q. Lian, K. Long, T. Zhou, H. Piao, A. Xu, H.X. Hui, K.K. Cheng, MDM2 induces pro-inflammatory and glycolytic responses in M1 macrophages by integrating iNOS-nitric oxide and HIF-1α pathways in mice, Nat. Commun. 15 (2024) 8624, https://doi.org/10.1038/s41467-024-53006-w.

[46] W. Wang, Y. Chu, Y. Lu, J. Xu, W. Zhao, Z. Liang, X. Guo, L. Xi, T. Han, Y. Shen, W. Song, Y. Tang, M. Wen, Z. Qian, L. Wang, Z. Fan, G. Zhou, W. Ren, Skatole Alleviates Osteoarthritis by Reprogramming Macrophage Polarization and Protecting Chondrocytes, vol. 8, 2025, p. 604, https://doi.org/10.34133/research.0604. Research (Washington, D.C.).

[47] Y. Ono, O. Yoshino, T. Hiraoka, E. Sato, Y. Fukui, A. Ushijima, A. Nawaz, Y. Hirota, S. Wada, K. Tobe, A. Nakashima, Y. Osuga, S. Saito, CD206+ M2-like macrophages are essential for successful implantation, Front. Immunol. 11 (2020) 557184, https://doi.org/10.3389/fimmu.2020.557184.

[48] W. Sha, B. Zhao, H. Wei, Y. Yang, H. Yin, J. Gao, W. Zhao, W. Kong, G. Ge, T. Lei, Astragalus polysaccharide ameliorates vascular endothelial dysfunction by stimulating macrophage M2 polarization via potentiating Nrf2/HO-1 signaling pathway, Phytomedicine : international journal of phytotherapy and phytopharmacology 112 (2023) 154667, https://doi.org/10.1016/j.phymed.2023.154667.

[49] X. Chen, Z. Wan, L. Yang, S. Song, Z. Fu, K. Tang, L. Chen, Y. Song, Exosomes derived from reparative M2-like macrophages prevent bone loss in murine periodontitis models via IL-10 mRNA, J. Nanobiotechnol. 20 (2022) 110, https://doi.org/10.1186/s12951-022-01314-y.

[50] A. Shapouri-Moghaddam, S. Mohammadian, H. Vazini, M. Taghadosi, S. A. Esmaeili, F. Mardani, B. Seifi, A. Mohammadi, J.T. Afshari, A. Sahebkar, Macrophage plasticity, polarization, and function in health and disease, J. Cell. Physiol. 233 (2018) 6425–6440, https://doi.org/10.1002/jcp.26429.

[51] V.A.K. Rathinam, Y. Zhao, F. Shao, Innate immunity to intracellular LPS, Nat. Immunol. 20 (2019) 527–533, https://doi.org/10.1038/s41590-019-0368-3.

[52] C. Oh, T.J. Spears, Y. Aachoui, Inflammasome-mediated pyroptosis in defense against pathogenic bacteria, Immunol. Rev. (2024), https://doi.org/10.1111/imr.13408.

[53] C.H. Lee, J.W. Choi, S1P/S1P(2) signaling Axis regulates both NLRP3 upregulation and NLRP3 inflammasome activation in macrophages primed with lipopolysaccharide, Antioxidants 10 (2021), https://doi.org/10.3390/antiox10111706.

[54] R. Muñoz-Planillo, P. Kuffa, G. Martínez-Colón, B.L. Smith, T.M. Rajendiran, G. Núñez, K^+ efflux is the common trigger of NLRP3 inflammasome activation by bacterial toxins and particulate matter, Immunity 38 (2013) 1142–1153, https://doi.org/10.1016/j.immuni.2013.05.016.

[55] J. Fu, K. Schroder, H. Wu, Mechanistic insights from inflammasome structures, Nat. Rev. Immunol. 24 (2024) 518–535, https://doi.org/10.1038/s41577-024-00995-w.

[56] M. Li, J. Yu, G. Guo, H. Shen, Interactions between macrophages and biofilm during Staphylococcus aureus-associated implant infection: difficulties and solutions, J. Innate Immun. 15 (2023) 499–515, https://doi.org/10.1159/000530385.

[57] J. Cao, L. Li, Y. Yao, Y. Xing, H. Ma, Dehydroepiandrosterone exacerbates nigericin-induced abnormal autophagy and pyroptosis via GPER activation in LPS-primed macrophages, Cell Death Dis. 13 (2022) 372, https://doi.org/10.1038/s41419-022-04841-6.

[58] J. Mei, X. Huang, C. Fan, J. Fang, Y. Jiu, Cytoskeleton network participates in the anti-infection responses of macrophage, Bioessays : news and reviews in molecular, cellular and developmental biology 45 (2023) e2200225, https://doi.org/10.1002/bies.202200225.